A&A 661, L2 (2022)
https://doi.org/10.1051/0004-6361/202243309

Astronomy & Astrophysics

LETTER TO THE EDITOR

NOEMA observations support a recoiling black hole in 3C 186

G. Castignani[1,2], E. Meyer[3], M. Chiaberge[4,5], F. Combes[6,7], T. Morishita[4,8], R. Decarli[2], A. Capetti[9], M. Dotti[10,11], G. R. Tremblay[12], and C. A. Norman[5,13]

[1] Dipartimento di Fisica e Astronomia "Augusto Righi", Alma Mater Studiorum Università di Bologna, Via Gobetti 93/2, 40129 Bologna, Italy
e-mail: gianluca.castignani@unibo.it
[2] INAF – Osservatorio di Astrofisica e Scienza dello Spazio di Bologna, Via Gobetti 93/3, 40129 Bologna, Italy
[3] University of Maryland Baltimore County, 1000 Hilltop Circle, Baltimore, MD 21250, USA
[4] Space Telescope Science Institute for the European Space Agency (ESA), ESA Office, 3700 San Martin Drive, Baltimore, MD 21218, USA
[5] The William H. Miller III Department of Physics & Astronomy, Johns Hopkins University, Baltimore, MD 21218, USA
[6] Observatoire de Paris, PSL University, Sorbonne University, CNRS, LERMA, 75014 Paris, France
[7] Collège de France, 11 Place Marcelin Berthelot, 75231 Paris, France
[8] Infrared Processing and Analysis Center, California Institute of Technology, MC 314-6, 1200 E. California Boulevard, Pasadena, CA 91125, USA
[9] INAF – Osservatorio Astrofisico di Torino, Via Osservatorio 20, 10025 Pino Torinese, Italy
[10] Università degli Studi di Milano-Bicocca, Piazza della Scienza 3, 30126 Milano, Italy
[11] INFN, Sezione di Milano-Bicocca, Piazza della Scienza 3, 30126 Milano, Italy
[12] Harvard-Smithsonian Center for Astrophysics, 60 Garden Street, Cambridge, MA 02138, USA
[13] Space Telescope Science Institute, 3700 San Martin Dr., Baltimore, MD 21210, USA

Received 11 February 2022 / Accepted 12 April 2022

ABSTRACT

3C 186 is a powerful radio-loud quasar (a quasi-stellar object) at the center of a cool-core cluster at $z = 1.06$. Previous studies have reported evidence for a projected spatial offset of $\sim 1''$ between the isophotal center of the galaxy and the point-source quasi-stellar object (QSO) as well as a spectral shift of $\sim 2000\,\mathrm{km\,s^{-1}}$ between the narrow and broad line region of the system. In this work we report high-resolution molecular gas CO(4→3) observations of the system taken with the NOEMA interferometer. We clearly detect a large reservoir of molecular gas, $M_{\mathrm{H_2}} \sim 8 \times 10^{10}\,M_{\odot}$, that is co-spatial with the host galaxy and likely associated with a rotating disk-like structure. We firmly confirm both the spatial offset of the galaxy's gas reservoir with respect to the continuum emission of the QSO and the spectral offset with respect to the redshift of the broad line region. Our morphological and kinematical analysis confirms that the most likely scenario to explain the 3C 186 system is that the QSO is a kicked super-massive black hole (SMBH), which we believe may have resulted from a strong gravitational wave recoil as two SMBHs coalesced after the merger of their host galaxies.

Key words. galaxies: active – quasars: individual: 3C186 – galaxies: jets – gravitational waves – galaxies: ISM – galaxies: star formation

1. Introduction

Galaxy mergers are fundamental mechanisms that regulate galaxy growth and the evolution of super-massive black holes (SMBHs) at their centers. The mergers of SMBHs are expected to be among the most energetic phenomena in the Universe, where a small fraction of the SMBH binding energy, $\frac{\Delta E}{M_{\bullet}c^2} \simeq 10^{-5}(\frac{M_{\bullet}}{10^6\,M_{\odot}})^{1/4}$, is converted into a large amount of gravitational wave (GW) radiation, $\sim 10^{55}\,\mathrm{erg}\,(\frac{M_{\bullet}}{10^6\,M_{\odot}})^{5/4}$ (Colpi 2014), where $M_{\bullet}$ is the black hole mass. Depending on both the relative orientation of the spins of the merging SMBHs and their mass ratio, the merged SMBH may receive a recoil kick (Centrella et al. 2010; Komossa 2012, for some reviews) with velocities as high as $\sim 5000\,\mathrm{km\,s^{-1}}$ (Campanelli et al. 2007; Lousto & Zlochower 2011), resulting from highly anisotropic GW radiation. With such a high velocity, the SMBH may be measurably displaced from the center of the host galaxy.

It is still debated how two SMBHs could reach the distance at which GW losses become important, the so-called final-parsec problem (e.g., Milosavljević & Merritt 2003). It is possible that SMBH pairs may stall and never merge, although a supply of torques from ambient gas may help in overcoming the problem. Simulations also show that even in gas-poor environments SMBH binaries can merge under certain conditions, for example if they formed in major galaxy mergers where the final galaxy is nonspherical (Bortolas et al. 2016; Khan et al. 2012; Preto et al. 2011). Observational evidence of unambiguous cases of galaxies that host GW-recoiling SMBHs would have a tremendous impact on our understanding of this process. Confirmed candidates are also important for future space-based missions such as the Evolved Laser Interferometer Space Antenna (eLISA) and pulsar-timing experiments (Amaro-Seoane et al. 2012; Klein et al. 2016; Kelley et al. 2018). They are sensitive to GWs of lower frequency (down to the nanohertz level) than those

associated with stellar-mass black hole mergers (from the hertz to the kilohertz level) detectable from ground-based interferometers such as Virgo and the Laser Interferometer Gravitational-Wave Observatory (LIGO; Abbott et al. 2021a,b). A confirmed recoiling SMBH candidate would provide evidence that SMBHs do in fact merge.

To that end, this work focuses on the recoiling SMBH candidate recently discovered in the radio-loud quasar 3C 186 (Chiaberge et al. 2017), at the center of a distant cool-core X-ray cluster at $z = 1.06$ (Siemiginowska et al. 2005, 2010). *Hubble* Space Telescope (HST) imaging shows that the bright quasar (a quasi-stellar object) in this system is offset by $1.3'' \pm 0.1''$ with respect to the host galaxy isophotal center (Hilbert et al. 2016; Chiaberge et al. 2017). New deep HST infrared Wide Field Camera 3 (WFC3) and optical Advanced Camera for Surveys (ACS) images confirm this spatial offset at high significance (Morishita et al. 2022). Furthermore, integral field spectroscopy with Keck shows evidence for blueshifted broad emission lines, with a significant velocity offset of $\sim$2000 km s^{-1} with respect to the narrow emission lines (Chiaberge et al. 2018).

It seems most likely that the narrow lines trace the more quiescent kinematics of the host galaxy. These lines are indeed produced in the narrow line region (NLR) on kiloparsec scales, far from the SMBH. Conversely, the broad line region (BLR) remains coupled to the recoiling SMBH (Loeb & Wyithe 2008), and thus the high relative velocity can be linked to the offset SMBH. An interpretation that self-consistently explains both spatial and spectral offsets is that the SMBH in 3C 186 is recoiling as a result of a gravitational radiation rocket effect following a major galaxy merger in which the central SMBHs merged. High-velocity (>1000 km s^{-1}) kicks are expected to be rare, but they are also more likely to be observed in combination with large spatial offsets such as the one we observe in 3C 186 (Lousto et al. 2012; Blecha et al. 2016).

If the GW recoil following a merger of two SMBHs is the correct interpretation, Lousto et al. (2017) showed that this would be the most energetic event ever observed: a major merger of progenitor SMBHs of comparable mass, giving rise to a highly spinning SMBH ($a = 0.91$), where $\sim$9% of the total mass is radiated as GWs. According to the GW-recoiling black hole scenario for 3C 186, we expect most of the molecular gas, which is the fuel of star formation, to have a redshift consistent with the narrow lines that we believe rest in the host galaxy frame (Chiaberge et al. 2017).

Chiaberge et al. (2017) already tested some alternatives to the GW recoil scenario: a dual active galactic nucleus (AGN), a pair of SMBHs, a double-peaked disk (e.g., Eracleous & Halpern 2003), or a quasar with extremely fast winds. However, none adequately explain both the spatial and the spectral offsets. Furthermore, recent deep HST observations by Morishita et al. (2022), supported by simulations, appear to exclude the possibility of a recent or ongoing merger.

The main goal of this work is to test the GW recoil hypothesis by mapping the cold gas reservoir in the 3C 186 system and determining its redshift. Observations similar to those presented in this work were vital for conclusively refuting the recoiling SMBH scenario in a different candidate source (J0927+2943 at $z = 0.7$; Decarli et al. 2014). The present study is part of a larger campaign to study the environmental processing of distant (brightest) cluster galaxies via CO observations (Castignani et al. 2018, 2019, 2020a,b,c,d).

Throughout this work we adopt a flat Λ cold dark matter cosmology with matter density $\Omega_m = 0.30$, dark energy density $\Omega_\Lambda = 0.70$, and Hubble constant $h = H_0/100\,\mathrm{km\,s^{-1}\,Mpc^{-1}} = 0.70$. The luminosity distance at the redshift of 3C 186, $z = 1.06$, is 7101 Mpc (i.e., $1'' = 8.11$ kpc).

2. NOEMA 1.8 mm observations and data reduction

We observed 3C 186 with the NOrthern Extended Millimeter Array (NOEMA) on 1, 5, and 10 March 2021, in A configuration, as part of the program W20CO (PI: Castignani). We used 10 antennas on 5 March and 11 antennas on the other two days of observations. With the 10- and 11-antenna configurations, the time spent on-source was 3.4 h and 8.2 h, respectively. The total observing time was 16.2 h (i.e., 11.6 h on source).

We set the phase center of the observations equal to the 3C 186 quasi-stellar object (QSO) coordinates, RA = 7^h:44^m:17.5^s and Dec = 37°:53′:17.2″. We used the PolyFix correlator, which covers a total bandwidth of 15.5 GHz, in each linear polarization, split between the lower sideband (LSB) and the upper sideband (USB). We adopted a tuning frequency in the upper inner baseband of 223.7 GHz, which is the mean between the redshifted CO(4→3) observed frequencies, ν_{obs}, for the NLR ($z = 1.068$, $\nu_{obs} = 222.940$ GHz) and the BLR ($z = 1.054$, $\nu_{obs} = 224.459$ GHz). With this tuning, the CO(4→3) lines of both the BLR and the NLR thus fall within the 3.9 GHz wide upper inner baseband.

The baseline range was 32–760 m. The program was executed in average, albeit unstable, winter weather conditions, with a system temperature $T_{sys} = 120$–250 K and a precipitable water vapor column of $\sim 1 - 3$ mm. The sources 0805+410 and 0738+313 were used as phase and amplitude calibrators, while 3C 84 and 3C 279 served as bandwidth and flux calibrators. We reduced the data using the clic package of the GILDAS software to obtain the final (u,v) tables.

We then imaged the visibilities using the MAPPING software of GILDAS. At the tuning frequency of 223.7 GHz, the half power primary beam width is 22.5″. We adopted natural weighting, which yielded a synthesized beam of $0.62'' \times 0.42''$ with PA = 14°. We then re-binned the spectral axis at a resolution of 53.61 km s^{-1} (i.e., 40 MHz at 223.7 GHz). At this resolution the resulting root mean square (rms) is 0.35 mJy beam^{-1}. As mentioned above, the frequency tuning was set to 223.7 GHz for our observations. However, in the following sections we always report velocities relative to the redshift of the NLR. With this convention, the CO(4→3) line for the NLR and BLR correspond to systemic velocities equal to 0 km s^{-1} and -2035.7 km s^{-1}, respectively.

3. Results

3.1. CO(4→3) emission

We clearly detect extended $2'' \times 2''$ CO(4→3) emission along the northeast direction at the NLR redshift, with a peak reached 0.6″ to the north and 1.3″ to the east of the quasar, at the coordinates (RA; Dec) = ($7^h44^m17.58^s$; 37°53′17.8″).

Figure 1 displays the HST WFC/F606W image of 3C 186 in its rest-frame ultraviolet (Morishita et al. 2022). The central QSO is co-spatial with the continuum emission at 1.3 mm (blue contours). The extended CO(4→3) emission is shown as green contours. Its peak is co-spatial with the isophotal center of the host galaxy (determined from 2D galaxy modeling; Chiaberge et al. 2017) and is clearly offset by 1.4″ to the NE of the central QSO. The CO emission extends down to the QSO itself in projection. It also partially overlaps with a star forming

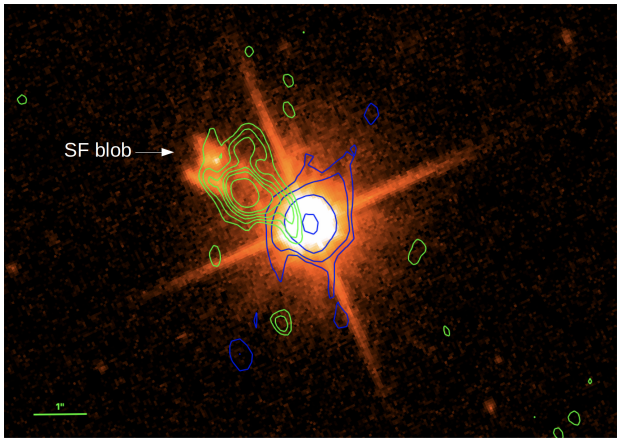

Fig. 1. HST WFC/F606W image (rest-frame UV) of 3C 186. Blue contours show the 1.3 mm continuum emission from the QSO, at levels of 0.10, 0.16, 0.40, and 1.34 mJy beam^{-1}. Green contours correspond to the CO(4→3) emission at levels of 183, 244, 305, 366, 427, and 549 mJy km s^{-1} beam^{-1}. The CO(4→3) emission is at the NLR redshift, redshifted by ∼2000 km s^{-1} with respect to the BLR that is co-spatial with the quasar. North is up, and east is to the left. The SF blob to the NE is highlighted.

(SF) blob to the NE (Hilbert et al. 2016), which is highlighted in Fig. 1.

Panels a, b, and c of Fig. A.1 show moment 0, 1, and 2 maps that display the CO(4→3) detection and were obtained after subtracting the continuum emission. The intensity map shows the CO(4→3) emission, with its peak clearly shifted by 1.4″ to the northeast from the 3C 186 quasar coordinates. The total emitting region is partially resolved by our observations. The intensity map shows evidence for a northern component connected to the main emitting region and a southern trail (hereafter denoted as the southern component) that extends to the southwest, almost reaching the position of the 3C 186 quasar. These two components are denoted as *N* and *S* in Fig. A.1a. Not only do they show up as morphological extensions of the main CO-emitting region in the intensity map, but they also appear to have distinct kinematics, as further discussed in Sect. 3.2. In the velocity map (Fig. A.1b) we highlight both the *N* and *S* components, centered at (RA; Dec) = ($7^h44^m17.56^s$; 37°53′18.7″) and ($7^h44^m17.52^s$;37°53′17.4″), respectively.

In panel a of Fig. A.2 we report the CO(4→3) spectrum for the total emitting region. In panels b and c we report CO(4→3) spectra for the northern and southern components separately. For the total system, our Gaussian fit yields a high signal-to-noise ratio (S/N) of 19, corresponding to a velocity integrated flux $S_{\mathrm{CO(4\to3)}}\Delta v = (2.09 \pm 0.11)$ Jy km s^{-1}, a full width at half maximum FWHM = (269 ± 17) km s^{-1}, and a redshift of 1.06811 ± 0.00005. The redshift is fully consistent with that of the narrow forbidden emission lines of the host galaxy from the literature (i.e., $z = 1.0685 \pm 0.0004$; Chiaberge et al. 2017; Hewett & Wild 2010).

Our observations are sensitive to the CO(4→3) line from sources within a 22.5 arcsec radius (i.e., 180 kpc) of the 3C 186 QSO, while the USB covers a broad velocity range of ∼(−8000; +2000) km s^{-1} with respect to the host galaxy (i.e., the NLR). Therefore, additional lines could have been serendipitously detected from companion cluster members. However, we inspected the entire datacube and detected no other emission line in the USB nor in the LSB. The two bands are sensitive to CO(4→3) from sources at redshifts $z = 1.01-1.08$ and $z = 1.16-1.24$, respectively.

3.2. CO(4→3) kinematics

The velocity map reported in Fig. A.1b shows that the bulk of the emitting region has a negligible velocity shift with respect to the NLR of the host galaxy. Both the northern and southern components instead have a velocity of up to ∼+100 km s^{-1} relative to the NLR, which implies that both slightly recede along the line of sight with respect to the main emitting region and are mainly distributed in the projected space. Such a moderate velocity shift for the two components implies a velocity gradient along the east-west direction; this suggests the presence of a mildly inclined disk-like structure, which, however, shows complex and disturbed morphology and kinematics.

The moment 2 map in Fig. A.1c shows that there are no strong gradients in the velocity width over the projected extension of the emitting region. The CO(4→3) line width ranges from (189^{+309}_{-126}) km s^{-1} over the entire emitting region, where the median value is reported along with the 68% interval. The highest values are found close to the location of the intensity peak, as in Fig. A.1a. This result is consistent with the presence of an SF disk-like structure. Indeed, the molecular gas reservoir typically shows an exponentially declining density profile and is thus quite concentrated at the galaxy center (Nishiyama et al. 2001; Regan et al. 2001; Leroy et al. 2008).

3.3. Continuum emission

By using the full LSB and the full USB separately, we looked for continuum emission, which we clearly detect in both sidebands and with similar flux densities. Figure A.1d and the blue contours of Fig. 1 display the continuum map in the LSB, which reveals a strong point-like component down to a 5σ significance level (rms = 0.03 mJy beam^{-1}), co-spatial with the 3C 186 QSO. There is also evidence of more extended emission down to a 3σ significance, which appears to be elongated along the NW-SE direction, similarly to the larger-scale Very Large Array (VLA) radio jet (Hilbert et al. 2016). By integrating over the region around the QSO delimited by the 5σ and 3σ contours, we find flux densities of 2.7 ± 0.1 mJy and 3.7 ± 0.2 mJy, respectively. This implies that the point-like source is dominant and accounts for ∼70% of the total emission around the QSO.

Figure A.1e displays the cleaned map of the residuals, where we have removed the central point-like component in the *uv*-visibility plane, assuming a Gaussian model. A fit with MAPPING yields a full width at half power FWHP = 0.28″, which is similar to the beam size. Extended features at a level of 3σ around the QSO, likely originated by the jet emission, are visible in the map. The nonthermal origin of the observed continuum emission is further strengthened when we compare the 1.3 mm continuum flux density with the total flux density of (1.31 ± 0.07) Jy at 1.4 GHz (Laing & Peacock 1980). We infer a spectral index $\alpha = 1.2 \pm 0.1$, which is typical of synchrotron emission $S_\nu \propto \nu^{-\alpha}$ of steep-spectrum radio-loud quasars such as 3C 186.

Furthermore, the QSO is co-spatial with a flat-spectrum component (K1), identified by Spencer et al. (1991) via high-resolution $\lesssim$0.03″ observations at 1.6 GHz, with a corresponding flux density of ∼12 mJy. Our observations instead have a spatial resolution of ∼0.5″, so we cannot spatially resolve the nonthermal emission of the core from that of the one-sided jet along the northwest direction (Spencer et al. 1991). However, combining

Table 1. CO(4→3) results for the total emitting region, denoted as "Total", as well as for the northern and southern components.

Component	$S_{\mathrm{CO(4\to3)}}$ (Jy km s^{-1})	FWHM (km s^{-1})	$L'_{\mathrm{CO(4\to3)}}$ (10^9 K km s^{-1} pc^2)	z	Velocity (km s^{-1})
Total	2.09 ± 0.11	269 ± 17	7.94 ± 0.42	1.06811 ± 0.00005	16 ± 7
North	0.20 ± 0.03	267 ± 47	0.76 ± 0.11	1.0684 ± 0.0004	57 ± 22
South	0.22 ± 0.03	304 ± 52	0.84 ± 0.11	1.0685 ± 0.0001	76 ± 19

the 1.6 GHz (K1) and 1.3 mm continuum emissions still yields a steep spectrum with $\alpha \simeq 0.3$, although this is flatter than that obtained using the total 1.4 GHz flux density. All these results suggest that the 1.3 mm continuum emission likely includes the contribution of both the core and the more extended jet.

3.4. Molecular gas reservoir

We estimated a total velocity integrated luminosity of $L'_{\mathrm{CO(4\to3)}} = (7.94 \pm 0.42) \times 10^9$ K km s^{-1} pc^2 using the following formula taken from Solomon & Vanden Bout (2005):

$$\frac{L'_{\mathrm{CO(4\to3)}}}{\mathrm{K\,km\,s^{-1}\,pc^2}} = 1.53 \times 10^2 \frac{S_{\mathrm{CO(4\to3)}}\,\Delta v}{\mathrm{Jy\,km\,s^{-1}}} \left(\frac{D_{\mathrm{L}}}{\mathrm{Mpc}}\right)^2 (1+z)^{-1}\,, \quad (1)$$

where D_{L} is the luminosity distance at the redshift (z) of the source. Similarly, we derived molecular gas properties for the northern and southern components separately from the fits reported in Fig. A.2.

Each of these two components is clearly detected at $S/N \simeq 7$ and accounts for ∼10% of the total observed emission. The best-fit results are summarized in Table 1. As reported in the table, the total, northern, and southern components have similar redshifts, fairly consistent with each others' within the errors bars, and similar line widths in the range ∼269−304 km s^{-1}, which is typical for massive galaxies. However, as further discussed in Sect. 3.2, both the northern and southern components have higher recession velocities than the total emitting system.

We then estimated the H_2 molecular gas mass as $M_{\mathrm{H_2}} = \alpha_{\mathrm{CO}} L'_{\mathrm{CO(4\to3)}}/r_{41}$ by assuming an excitation ratio of $r_{41} = L'_{\mathrm{CO(4\to3)}}/L'_{\mathrm{CO(1\to0)}} = 0.41$ (Bothwell et al. 2013; Carilli & Walter 2013), typical of submillimeter galaxies. We adopted a Galactic CO-to-H_2 conversion factor, $\alpha_{\mathrm{CO}} = 4.36\,M_\odot\,(\mathrm{K\,km\,s^{-1}\,pc^2})^{-1}$, typical of main sequence (MS) SF galaxies. This choice is reasonable as the 3C 186 system has a star formation rate (SFR) that is typical of MS galaxies, as further discussed in Sect. 4.

We obtain a total high H_2 gas mass of $(8.4 \pm 0.4)\,10^{10}\,M_\odot$ as well as $M_{\mathrm{H_2}} \simeq (8-9)\times10^9\,M_\odot$ for both the N and S components. In Fig. A.2d we report the CO(4→3) spectrum extracted at the location of the QSO (i.e., the phase center of the observations), which shows no emission line at the BLR redshift. We used this spectrum to estimate, at a resolution of 300 km s^{-1}, a 3σ upper limit of $S_{\mathrm{CO(4\to3)}} < 0.17$ Jy km s^{-1}, which corresponds to $M_{\mathrm{H_2}} < 6.8 \times 10^9\,M_\odot$.

3.5. Dust mass

Podigachoski et al. (2015) reported evidence for near- to far-infrared emission in 3C 186, between 3.6 µm and 70 µm in the observer frame, as well as *Herschel* upper limits at longer wavelengths. By modeling the spectral energy distribution (SED), the authors then derived a conservative upper limit to the infrared (IR) luminosity of 3C 186, $L_{\mathrm{IR}} < 5 \times 10^{11}\,L_\odot$, which we used to set an upper limit to the dust mass (e.g., Beelen et al. 2006):

$$M_{\mathrm{dust}} = \frac{L_{\mathrm{IR}}}{4\pi \int \kappa(\upsilon) B(\upsilon, T_{\mathrm{dust}})\,\mathrm{d}\upsilon} < 1.9 \times 10^8\,M_\odot, \quad (2)$$

where $\kappa(\upsilon) = \kappa_0 \cdot (\upsilon/\upsilon_0)^\beta$ is the dust opacity per unit mass of dust, and $B(\upsilon, T)$ is the spectral radiance of a black body of temperature T at frequency υ.

To derive the M_{dust} upper limit reported in Eq. (2), we adopted $\kappa_0 = 0.4\,\mathrm{cm^2\,g^{-1}}$ at $\nu_0 = 250$ GHz (Beelen et al. 2006; Alton et al. 2004, and references therein), $\beta = 1.8$ (Scoville et al. 2017), and a dust temperature $T_{\mathrm{dust}} = 30$ K, which we inferred using the T_{dust} vs. L_{IR} scaling relation for MS galaxies by Magnelli et al. (2020).

Under the assumption that molecular gas is shielded by a dust reservoir that is extended over a projected area similar to that of the CO, a dust continuum emission offset from the QSO would have been clearly detectable with our observations in the Rayleigh-Jeans regime. As further discussed in Sect. 3.3, the observed continuum is instead co-spatial with the QSO, with only some ∼3σ features toward the CO-emitting region. Integrating the continuum map of the residuals (Fig. A.1e) over the extent of the CO-emitting region yields a continuum density flux of ∼0.4 mJy, which we used to estimate an upper limit to the dust mass: $M_{\mathrm{dust}} < 2.0 \times 10^8\,M_\odot$. To estimate this upper limit, we followed Eq. (A.6) of Castignani et al. (2020a) and adopted the same dust temperature and opacity parameters used above in Eq. (2).

This continuum-based M_{dust} upper limit is in excellent agreement with that of Eq. (2). We then obtain an H_2-to-dust mass ratio of $M_{\mathrm{H_2}}/M_{\mathrm{dust}} \gtrsim 400$ for the system, higher than the values of ∼100 typically found for distant SF galaxies (Berta et al. 2016; Scoville et al. 2014, 2016).

We stress that AGN emission may affect our estimates, leading to biased-high, and thus conservative, M_{dust} upper limits. Lower values would increase the $M_{\mathrm{H_2}}/M_{\mathrm{dust}}$ ratio and thus the tension mentioned above. A CO-to-H_2 conversion factor lower than the Galactic one used in this work would instead alleviate the tension. Indeed, assuming an $\alpha_{\mathrm{CO}} = 0.8\,M_\odot\,(\mathrm{K\,km\,s^{-1}\,pc^2})^{-1}$, more typical of starbursts, the $M_{\mathrm{H_2}}/M_{\mathrm{dust}}$ ratio is reduced by a factor of ∼5.5.

Alternatively, to explain the large $M_{\mathrm{H_2}}/M_{\mathrm{dust}}$ ratio, it could be that a substantial fraction of the observed gas reservoir has been accreted by the galaxy as a result of a past merger. Ratios of several hundred have in fact been commonly found in merger remnants (Davis et al. 2015). Indeed, Chiaberge et al. (2017) suggested that the 3C 186 system is in a late merger phase (∼1 Gyr old) based on a comparison with numerical simulations. This interpretation is in agreement with the stellar population age being ≳200 Myr, as inferred by Morishita et al. (2022) on the basis of a stellar population analysis. The stellar, gas, and dust properties of the system are listed in Table 2.

Table 2. Stellar, gas, and dust properties of the 3C 186 system.

$M_\star$	$(2.04^{+0.59}_{-0.18}) \times 10^{11}\,M_\odot$
$M_\star$ (NE SF blob)	$7.94 \times 10^9\,M_\odot$
$\mathrm{SFR_{IR}}$	$<80\,M_\odot\,\mathrm{yr}^{-1}$
$\mathrm{SFR_{SED}}$	$(65 \pm 20)\,M_\odot\,\mathrm{yr}^{-1}$
$M_{\mathrm{H_2}}$	$(8.4 \pm 0.4) \times 10^{10}\,M_\odot$
$M_{\mathrm{H_2}}/M_\star$	$0.41^{+0.04}_{-0.12}$
M_{dust}	$<1.9 \times 10^8\,M_\odot$ (IR)
	$<2.0 \times 10^8\,M_\odot$ (1.3 mm continuum)
$M_{\mathrm{H_2}}/M_{\mathrm{dust}}$	$\gtrsim 400$
$\tau_{\mathrm{dep}} = M_{\mathrm{H_2}}/\mathrm{SFR}$	(1.3 ± 0.4) Gyr

4. Discussion and conclusions

The scenario that emerges from our analysis is that we detect a large molecular gas reservoir over a ∼16 kpc scale region, likely associated with a disk-like structure of a massive galaxy. Similar complex morphology and kinematics are observed in both distant and local cluster core galaxies (e.g., Russell et al. 2019; Noble et al. 2019). With this work we confirm both the spatial and velocity offset found in previous studies with respect to the BLR of the QSO. These findings confirm the 3C 186 system as an excellent candidate for a kicked SMBH that resulted from a strong GW recoil as two SMBHs coalesced after the merger of their host galaxies. The present study thus reports the first confirmation of a GW recoil candidate via high-resolution millimeter observations.

Rest frame optical-UV SED modeling by Morishita et al. (2022) found that the SF blob dominates the total star formation of the system, with an estimated $\mathrm{SFR} = (65 \pm 20)\,M_\odot\,\mathrm{yr}^{-1}$; this is in good agreement with the upper limit to the total $\mathrm{SFR} < 80\,M_\odot\,\mathrm{yr}^{-1}$ as estimated by Podigachoski et al. (2015), who modeled the near- to far-IR photometry of 3C 186. Conversely, the SED analysis by Morishita et al. (2022) shows that the SF blob contributes only 4% of the total stellar mass, $M_\star = (2.04^{+0.59}_{-0.18}) \times 10^{11}\,M_\odot$, of the system.

The estimated SFR is consistent with that of MS field galaxies, $\mathrm{SFR_{MS}} = 76\,M_\odot\,\mathrm{yr}^{-1}$ (Speagle et al. 2014), with $M_\star$ and the redshift equal to those of 3C 186. These findings support our choice for a Galactic CO-to-H_2 conversion factor, while a lower α_{CO} would be more appropriate for more SF galaxies with SFR> 3 $\mathrm{SFR_{MS}}$. The system is not only massive, but also gas rich. Our observations yield a H_2-to-stellar-mass ratio of $M_{H_2}/M_\star = 0.41^{+0.04}_{-0.12}$, well in agreement with the MS values for field galaxies, $(M_{\mathrm{H_2}}/M_\star)_{\mathrm{MS}} = 0.30 \pm 0.20$, with $M_\star$ and the redshift equal to those of 3C 186 (Tacconi et al. 2018).

Under the assumption that the H_2-to-stellar mass ratio reflects that of field galaxies, we can express the ratio as $M_{\mathrm{H_2}}/M_\star \sim 0.1\,(1+z)^2$ (Carilli & Walter 2013). This yields $M_\star < 1.6 \times 10^{10}\,M_\odot$, which is the upper limit to the stellar mass of the QSO host galaxy if the quasar host is superimposed in projection onto the brighter offset galaxy. The QSO host should then be of low mass, which is quite unlikely for a radio-loud AGN at the cluster center because (i) the hosts of radio-loud QSOs are typically massive ellipticals, with $M_\star$ largely exceeding $10^{10}\,M_\odot$, and, similarly, (ii) cluster cores are predominantly populated by massive galaxies. The possibility that the 3C 186 QSO is hosted by an under-massive galaxy is thus quite unlikely, as previously argued by Chiaberge et al. (2017) on the basis of the $M_\star - M_\bullet$ relation.

Furthermore, we estimate a depletion timescale of $\tau_{\mathrm{dep}} = M_{\mathrm{H_2}}/\mathrm{SFR} = 1/\mathrm{SFE} = (1.3 \pm 0.4)$ Gyr (where SFE is the star formation efficiency), which is slightly higher than that predicted for field MS galaxies, $\tau_{\mathrm{dep,MS}} = (0.93^{+0.18}_{-0.15})$ Gyr, at a given $M_\star$ and redshift (Tacconi et al. 2018). This implies a relatively low star formation efficiency for the system: part of the H_2 reservoir may be recently accreted and is not being converted effectively into stars, an interpretation that is in agreement with the occurrence of a past merger (Sect. 3.5).

Throughout our analysis we adopted a Galactic CO-to-H_2 conversion factor. The possibility of instead having a lower $\alpha_{\mathrm{CO}} = 0.8\,M_\odot\,(\mathrm{K\,km\,s^{-1}\,pc^2})^{-1}$, typical of starbursts, cannot be firmly excluded. However, it would lead to a relatively low $M_{\mathrm{H_2}}/M_\star \simeq 0.08$ and a short $\tau_{\mathrm{dep}} \simeq 0.2$ Gyr with respect to the MS predictions.

While the bulk of the CO emission is co-spatial with the host galaxy isophotal center, we observe an offset with respect to the northeastern SF blob, as often found in high-z brightest cluster galaxies (BCGs; Strazzullo et al. 2018; D'Amato et al. 2020). It is likely that a large fraction of the rest-frame UV emission of the galaxy is obscured by dust, and thus not seen in Fig. 1, consistent with the non-negligible far-IR emission reported by Podigachoski et al. (2015).

It is also possible that we are tracing only the most dense and central regions of the gas reservoir and that lower-J CO emission could reveal a more extended gas reservoir. We indeed find evidence for diffuse $S/N \lesssim 3$ emission that is coherently distributed along the periphery of the emitting region (Figs. A.1a and 1). An alternative explanation is that part of the observed extended emission is associated with the diffuse circumgalactic medium. However, we think this is less likely, as we would expect much larger line widths, more complex line kinematics, and extended emission over tens of kiloparsecs or more (Emonts et al. 2016; Ginolfi et al. 2017; Cicone et al. 2021).

Overall, our study reveals a large molecular gas reservoir that is likely associated with a rotating disk but is still forming, as suggested by the observed complex kinematics and mutliple components. Indeed, the highest-velocity gradients (Fig. A.1b) are found between the central part of the emitting region and the adjacent northern and southern components. The southern component recedes along the line of sight with respect to both the bulk of the gas reservoir and the central quasar, and its end appears blueshifted. These gradients suggest that the southern component may be a disk component that is torqued (e.g., a tidal tail), possibly due to past dynamical interactions. Interestingly, similar complex features and kinematics are often observed in merger remnants (Ueda et al. 2014). It is thus possible that the observed molecular emitting gas is associated with a disk in formation.

The two morphological extensions of the main CO-emitting region (i.e., the N and S components; Sect. 3) are thus reminiscent of a strong environmental processing of the gas occurring in the cluster core. The cool-core cluster environment may favor the condensation and the inflow of the intracluster medium gas toward the cluster center, as found only for some local (Salomé et al. 2006; Tremblay et al. 2016) and intermediate-z BCGs (Castignani et al. 2020c). Such a condensation is manifested by means of the significant molecular gas reservoir that we observe in the 3C 186 system, which is possibly regulated by radio-mode AGN feedback originated by the nonthermal emission of the QSO. In 3C 186 we thus witness the assembly of a high-z progenitor of local BCGs in great detail at a much higher resolution compared to other recent studies (Castignani et al. 2020a; D'Amato et al. 2020).

In conclusion, the projected and spectral offsets of the molecular gas reservoir with respect to the BLR of the QSO, as well as the complex morphology and kinematics of the 3C 186 system, presented in this study strongly support the scenario that 3C 186 is a result of a GW recoil following a past merger. The system is an excellent target for follow-up observations with the *James Webb* Space Telescope.

Acknowledgements. We thank the anonymous referee for helpful comments which contributed to improve the paper. This work is based on observations carried out under project number W20CO with the IRAM NOEMA Interferometer. IRAM is supported by INSU/CNRS (France), MPG (Germany) and IGN (Spain). GC thanks Melanie Krips and all IRAM staff for the observations and help concerning the data reduction. GC acknowledges the support from the grant ASI n.2018-23-HH.0. The authors thank Bryan Hilbert and Erini Lambrides for helpful discussion. The imaging data of HST/ACS F606W in Fig. 1 was taken in the HST GO-15254 program and processed in Morishita et al. (2022).

References

Abbott, R., Abbott, T. D., Abraham, S., et al. 2021a, Phys. Rev. X, 11, 1053
Abbott, R., Abbott, T. D., Acernese, F., et al. 2021b, ArXiv e-print [arXiv:2111.03606]
Alton, P. B., Xilouris, E. M., Misiriotis, A., et al. 2004, A&A, 425, 109
Amaro-Seoane, P., Aoudia, S., Babak, S., et al. 2012, Class. Quant. Grav., 29, 4016
Beelen, A., Cox, P., Benford, D. J., et al. 2006, ApJ, 642, 694
Berta, S., Lutz, D., Genzel, R., et al. 2016, A&A, 587, A73
Blecha, L., Sijacki, D., Kelley, L. Z., et al. 2016, MNRAS, 456, 961
Bortolas, E., Gualandris, A., Dotti, M., et al. 2016, MNRAS, 461, 1023
Bothwell, M. S., Smail, I., Chapman, S. C., et al. 2013, MNRAS, 429, 3047
Campanelli, M., Lousto, C., Zlochower, Y., et al. 2007, Phys. Rev. L, 98, 1102
Carilli, C. L., & Walter, F. 2013, ARA&A, 51, 105
Castignani, G., Combes, F., Salomé, P., et al. 2018, A&A, 617, A103
Castignani, G., Combes, F., Salomé, P., et al. 2019, A&A, 623, A48
Castignani, G., Combes, F., & Salomé, P. 2020a, A&A, 635, L10
Castignani, G., Combes, F., Salomé, P., et al. 2020b, A&A, 635, A32
Castignani, G., Pandey-Pommier, M., Hamer, S. L., et al. 2020c, A&A, 640, A65
Castignani, G., Jablonka, P., Combes, F., et al. 2020d, A&A, 640, A64
Centrella, J., Baker, J. G., Kelly, B. J., et al. 2010, RvMP, 82, 3069
Chiaberge, M., Ely, J. C., Meyer, E. T., et al. 2017, A&A, 600, A57
Chiaberge, M., Tremblay, G. R., Capetti, A., et al. 2018, ApJ, 861, 56
Cicone, C., Mainieri, V., Circosta, C., et al. 2021, A&A, 654, L8
Colpi, M. 2014, Space Sci. Rev., 183, 189
D'Amato, Q., Gilli, R., & Prandoni, I. 2020, A&A, 641, L6
Davis, T. A., Rowlands, K., Allison, J. R., et al. 2015, MNRAS, 449, 3503
Decarli, R., Dotti, M., Mazzucchelli, C., et al. 2014, MNRAS, 445, 1558
Emonts, B. H. C., Lehnert, M. D., Villar-Martín, M., et al. 2016, Science, 354, 1128
Eracleous, M., & Halpern, J. P. 2003, ApJ, 599, 886
Ginolfi, M., Maiolino, R., Nagao, T., et al. 2017, MNRAS, 468, 3468
Hewett, P. C., & Wild, V. 2010, MNRAS, 405, 2302
Hilbert, B., Chiaberge, M., Kotyla, J. P., et al. 2016, ApJS, 225, 12
Kelley, L. Z., Blecha, L., Hernquist, L., et al. 2018, MNRAS, 477, 964
Khan, F. M., Preto, M., Berczik, P., et al. 2012, ApJ, 749, 147
Klein, A., Barausse, E., Sesana, A., et al. 2016, Phys. Rev. D, 93, 4003
Komossa, S. 2012, Adv. Astron., 14
Laing, R. A., & Peacock, J. A. 1980, MNRAS, 190, 903
Leroy, A. K., Walter, F., Brinks, E., et al. 2008, AJ, 136, 2782
Loeb, A., & Wyithe, J. S. B. 2008, Phys. Rev. L, 100, 1301
Lousto, C. O., & Zlochower, Y. 2011, Phys. Rev. L, 107, 1102
Lousto, C., Zlochower, Y., Dotti, M., et al. 2012, Phys. Rev. D, 85, 4015
Lousto, C. O., Zlochower, Y., & Campanelli, M. 2017, ApJ, 841, 28
Magnelli, B., Boogaard, L., Decarli, R., et al. 2020, ApJ, 892, 66
Nishiyama, K., Nakai, N., & Kuno, N. 2001, PASJ, 53, 757
Noble, A. G., Muzzin, A., McDonald, M., et al. 2019, ApJ, 870, 56
Milosavljević, M., & Merritt, D. 2003, ApJ, 596, 860
Morishita, T., Chiaberge, M., Hilbert, B., et al. 2022, ApJ, submitted
Podigachoski, P., Barthel, P. D., Haas, M., et al. 2015, A&A, 575, A80
Preto, M., Berentzen, I., Berczik, P., et al. 2011, ApJ, 732, 26
Regan, M. W., Thornley, M. D., Helfer, T. T., et al. 2001, ApJ, 561, 218
Russell, H. R., McNamara, B. R., Fabian, A. C., et al. 2019, MNRAS, 490, 3025
Salomé, P., Combes, F., Edge, A. C., et al. 2006, A&A, 454, 437
Scoville, N., Aussel, H., Sheth, K., et al. 2014, ApJ, 783
Scoville, N., Sheth, K., Aussel, H., et al. 2016, ApJ, 820, 83
Scoville, N., Lee, N., Vanden Bout, P., et al. 2017, ApJ, 837, 150
Siemiginowska, A., Cheung, C. C., LaMassa, S., et al. 2005, ApJ, 632, 110
Siemiginowska, A., Burke, D. J., Aldcroft, T. L., et al. 2010, ApJ, 722, 102
Solomon, P. M., & Vanden Bout, P. A. 2005, ARA&A, 43, 677
Speagle, J. S., Steinhardt, C. L., Capak, P. L., et al. 2014, ApJS, 214, 15
Spencer, R. E., Schilizzi, R. T., Fanti, C., et al. 1991, MNRAS, 250, 225
Strazzullo, V., Coogan, R. T., Daddi, E., et al. 2018, ApJ, 862, 64
Tacconi, L. J., Genzel, R., Saintonge, A., et al. 2018, ApJ, 853, 179
Tremblay, G. R., Oonk, J. B. R., Combes, F., et al. 2016, Nature, 534, 218
Ueda, J., Iono, D., Yun, M. S., et al. 2014, ApJS, 214, 1

Appendix A: NOEMA maps and spectra

Here we provide NOEMA maps and spectra. We refer to Sects. 3 and 4 for details and discussion.

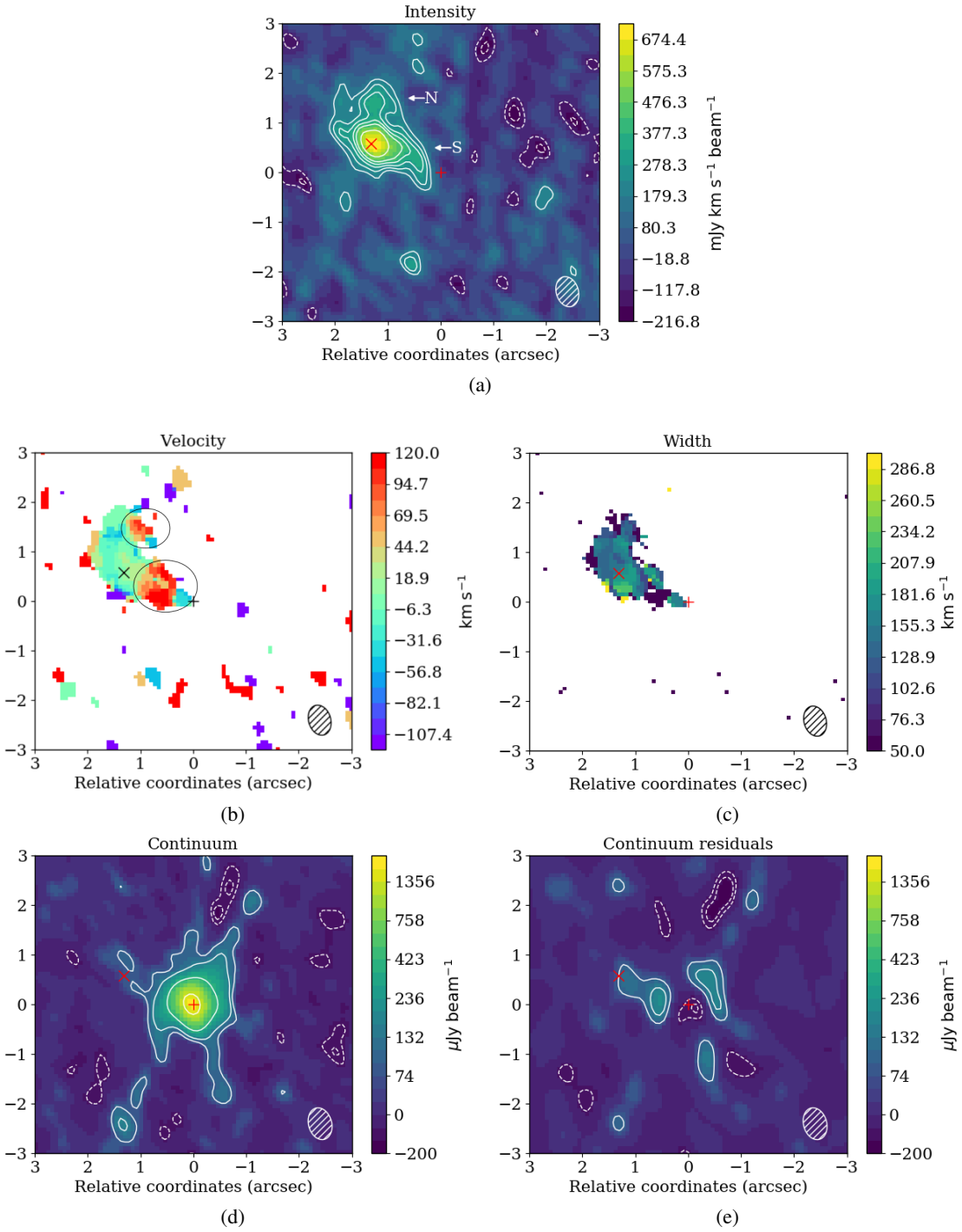

Fig. A.1. NOEMA maps. (a) Intensity, (b) velocity, and (c) velocity dispersion CO(4→3) maps derived from moments 0, 1, and 2, respectively. Panel (d) shows the continuum map in the LSB, and panel (e) displays the map of the residuals once the central point-like component has been removed. Coordinates are reported as angular separations from the phase center, i.e., the 3C 186 QSO coordinates. The phase center and the CO intensity peak are marked with the symbols + and x, respectively. The northern (N) and southern (S) components are highlighted with arrows (panel a) and ellipses (panel b). In the panels (a-c) the velocity range considered corresponds to the velocity support [-350; 330] km s^{-1} of the CO(4→3) line, while in panels (d, e) all the 7.7 GHz bandwidth of the LSB is used. Contour levels are superimposed onto both the intensity and continuum maps. They correspond to significance levels of -3, -2, 3, 4, 5, 6, 7, and 9σ (panel a) or -3, -2, 3, 5, 13, and 45σ (panels d, e). Dashed and solid contours refer to negative and positive significance levels, respectively. The dashed ellipses at the bottom right of each panel show the beam size.

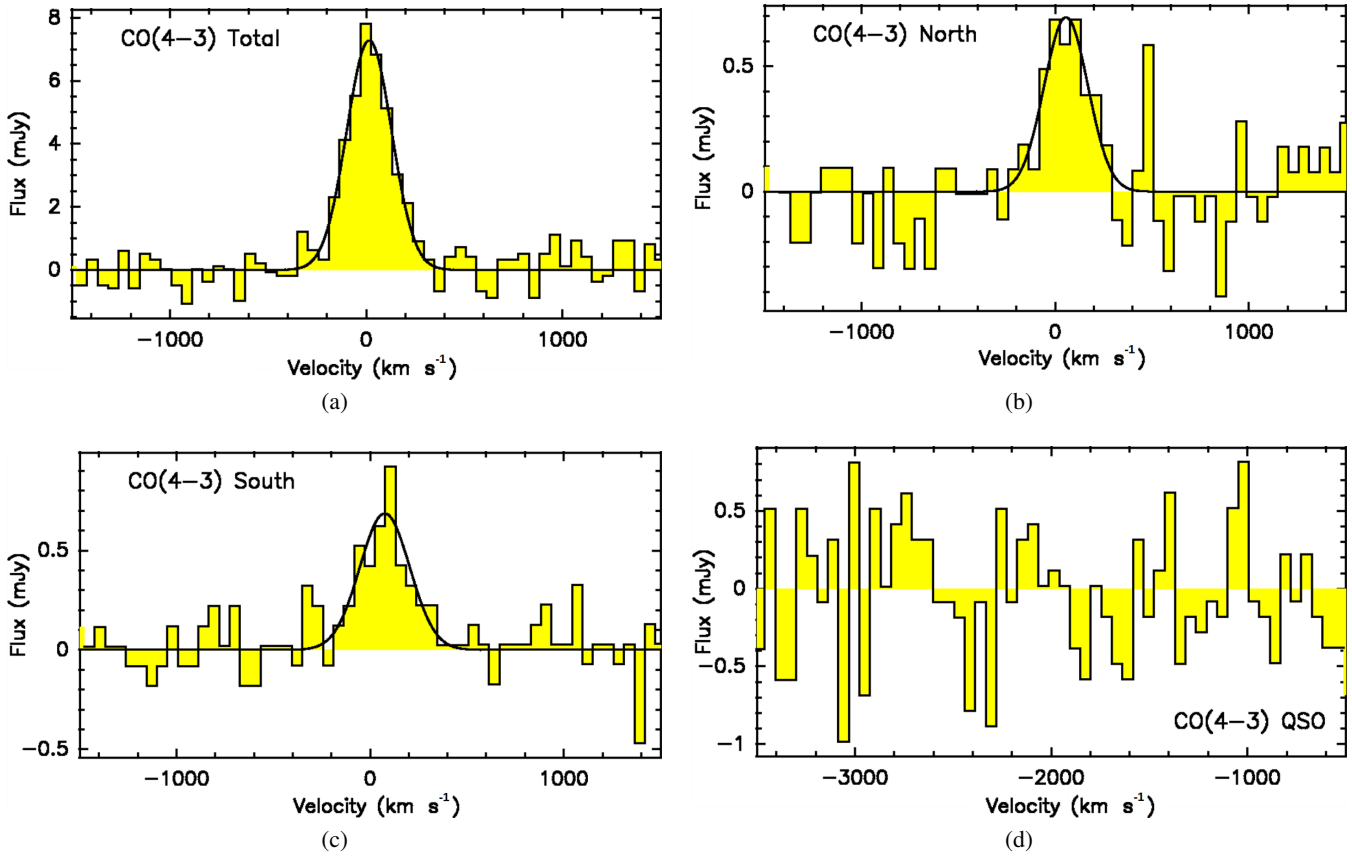

Fig. A.2. Baseline subtracted CO(4→3) spectra for the total emitting region (a), the northern component (b), the southern component (c), and the QSO (d). For the *N* and *S* components, we chose as regions of integration those denoted by the ellipses in Fig. A.1b, while for the QSO we chose a 1″ × 1″ region centered around it that corresponds fairly well to the extent of the continuum emission (Fig. A.1d). In panels (a), (b), and (c) the solid line shows the Gaussian best fit to the CO(4→3) line. Velocities, shown on the x axis, are evaluated with respect to the NLR redshift. The BLR is blueshifted to a velocity of -2035.7 km s^{-1}.